

# Confined local oxygen gas promotes electrochemical water oxidation to hydrogen peroxide

Chuan Xia<sup>1,2,9</sup>, Seoin Back<sup>3,9</sup>, Stefan Ringe<sup>3,9</sup>, Kun Jiang<sup>4</sup>, Fanhong Chen<sup>5</sup>, Xiaoming Sun<sup>5</sup>, Samira Siahrostami<sup>6\*</sup>, Karen Chan<sup>7\*</sup> and Haotian Wang<sup>1,8\*</sup>

**Electrochemical two-electron water oxidation is a promising route for renewable and on-site H<sub>2</sub>O<sub>2</sub> generation as an alternative to the anthraquinone process. However, it is currently restricted by low selectivity due to strong competition from the traditional four-electron oxygen evolution reaction, as well as large overpotential and low production rates. Here we report an interfacial engineering approach, where by coating the catalyst with hydrophobic polymers we confine in situ produced O<sub>2</sub> gas to tune the water oxidation reaction pathway. Using carbon catalysts as a model system, we show a significant increase of the intrinsic H<sub>2</sub>O-to-H<sub>2</sub>O<sub>2</sub> selectivity and activity compared to that of the pristine catalyst. The maximal H<sub>2</sub>O<sub>2</sub> Faradaic efficiency was enhanced by sixfold to 66% with an overpotential of 640 mV, under which a H<sub>2</sub>O<sub>2</sub> production rate of 23.4 μmol min<sup>-1</sup> cm<sup>-2</sup> (75.2 mA cm<sup>-2</sup> partial current) was achieved. This approach was successfully extended to nickel metal, demonstrating the wide applicability of our local gas confinement concept.**

Hydrogen peroxide (H<sub>2</sub>O<sub>2</sub>) is one of the most important fundamental chemicals in the modern chemical engineering industry as well as energy and environmental applications, with an annual global demand of about 4 million tons<sup>1–6</sup>. It is currently produced through the energy-demanding and waste-intensive anthraquinone cycling process<sup>7</sup>, which is only economically viable on a relatively large scale and relies heavily on transportation and storage of unstable and hazardous bulk H<sub>2</sub>O<sub>2</sub> solutions<sup>8</sup>. Using renewable electricity for on-site H<sub>2</sub>O<sub>2</sub> generation via electrocatalytic processes has recently emerged as a promising alternative to the traditional method<sup>9–14</sup>, with significant advantages including ambient reaction conditions, a renewable energy source without fossil fuels, and green precursors such as water and air. As the oxidation state of oxygen (–1) in H<sub>2</sub>O<sub>2</sub> sits between molecular oxygen and water, there are two possible ways for electrochemical H<sub>2</sub>O<sub>2</sub> generation: the first starts from O<sub>2</sub> via the two-electron oxygen reduction reaction (2e<sup>-</sup>-ORR); the other starts from H<sub>2</sub>O via the 2e<sup>-</sup> water oxidation reaction (2e<sup>-</sup>-WOR; E<sup>0</sup> = 1.76 V versus normal hydrogen electrode)<sup>13</sup>. Both 2e<sup>-</sup> pathways, however, compete with their otherwise 4e<sup>-</sup> counterparts towards H<sub>2</sub>O and O<sub>2</sub>, respectively. While exciting progress has been made in developing highly selective catalysts for ORR towards H<sub>2</sub>O<sub>2</sub> instead of H<sub>2</sub>O (refs. 9–11,15,16), there are very few known catalysts that can selectively and actively oxidize H<sub>2</sub>O into H<sub>2</sub>O<sub>2</sub> with stable performances<sup>12,13,17,18</sup>. Most reported water oxidation catalysts, such as metal oxides, hydroxides, chalcogenides, nitrides and carbon materials, show exclusive oxygen evolution reaction (OER) under water oxidation potentials<sup>19–25</sup>. Steering the regular 4e<sup>-</sup>-WOR pathway towards the unconventional 2e<sup>-</sup>

pathway therefore becomes both fundamentally interesting for mechanistic understanding, and technologically important as a promising anode route for H<sub>2</sub>O<sub>2</sub> generation. In addition, the development of high-performance 2e<sup>-</sup>-WOR catalysts, coupled with the corresponding 2e<sup>-</sup>-ORR cathode catalysts, will enable an efficient H<sub>2</sub>O<sub>2</sub> electrosynthetic cell where H<sub>2</sub>O<sub>2</sub> can be selectively generated from both electrodes.

The key in tuning the WOR pathway relies on the interaction between the catalytic surface and O intermediates, such as \*O, \*OH and \*OOH (refs. 13,26). In general, a proper interaction is desired for selective and active 2e<sup>-</sup>-WOR: too strong an OH binding could further oxidize \*OH to \*O and \*OOH, finishing the complete 4e<sup>-</sup> oxidation pathway towards O<sub>2</sub>; too weak a binding will lead to high kinetic barriers of water dissociation, dramatically slowing down the reaction rate<sup>13</sup>. Previous efforts have been focused on screening catalytic materials with proper electronic structures, such as wide-band-gap metal oxides (ZnO, WO<sub>3</sub>, SnO<sub>2</sub>, TiO<sub>2</sub>, BiVO<sub>4</sub> and CaSnO<sub>3</sub>)<sup>13,14,18,27</sup>. While promising progress has been made in improving H<sub>2</sub>O<sub>2</sub> selectivity, the state-of-the-art catalysts still present significant overpotentials of more than 1 V to deliver relatively low H<sub>2</sub>O<sub>2</sub> partial currents (~10 mA cm<sup>-2</sup>)<sup>13,14,18,27</sup>. Unlike the screening method for these materials for improving the performance of 2e<sup>-</sup>-WOR, we propose to use locally generated O<sub>2</sub> gas, from the catalysts' surface, to effectively regulate the interaction with O intermediates and thus change the reaction selectivity and activity. Under a positive enough potential, most of the water oxidation catalysts will continuously evolve O<sub>2</sub> with their active sites refreshed after the generated O<sub>2</sub> gas bubbles away<sup>28</sup>. We hypothesize that, if those generated O<sub>2</sub>

<sup>1</sup>Department of Chemical and Biomolecular Engineering, Rice University, Houston, TX, USA. <sup>2</sup>Smalley-Curl Institute, Rice University, Houston, TX, USA.

<sup>3</sup>SUNCAT Center for Interface Science and Catalysis, Department of Chemical Engineering, Stanford University, Stanford, CA, USA. <sup>4</sup>School of Mechanical Engineering, Shanghai Jiaotong University, Shanghai, China. <sup>5</sup>State Key Laboratory of Chemical Resource Engineering, College of Energy, and Beijing Advanced Innovation Centre for Soft Matter Science and Engineering, Beijing University of Chemical Technology, Beijing, China. <sup>6</sup>Department of Chemistry, University of Calgary, Calgary, Alberta, Canada. <sup>7</sup>Department of Physics, Technical University of Denmark, Kongens Lyngby, Denmark.

<sup>8</sup>Canadian Institute for Advanced Research, Toronto, Ontario, Canada. <sup>9</sup>These authors contributed equally: Chuan Xia, Seoin Back, Stefan Ringe.

\*e-mail: [samira.siahrostami@ucalgary.ca](mailto:samira.siahrostami@ucalgary.ca); [kchan@fysik.dtu.dk](mailto:kchan@fysik.dtu.dk); [htwang@rice.edu](mailto:htwang@rice.edu)

gas can be confined around the active sites, the accumulated O<sub>2</sub> molecules could further interact with the catalysts' surface or the intermediate O species, and thus be able to tune the intermediate binding strength for completely different reaction pathways.

Here we report an interfacial engineering approach in which we trap in situ produced O<sub>2</sub> gas close to active sites by coating the catalyst surface with hydrophobic polymers. Using OER-selective carbon catalysts as a model system, we observed a significant increase of the intrinsic H<sub>2</sub>O-to-H<sub>2</sub>O<sub>2</sub> selectivity and activity once generated O<sub>2</sub> gas was confined to the surface. The H<sub>2</sub>O<sub>2</sub> selectivity was enhanced by sixfold from only 11% on pristine carbon to a maximal of 66%. An H<sub>2</sub>O<sub>2</sub> production rate of 23.4 μmol min<sup>-1</sup> cm<sup>-2</sup> (75.2 mA cm<sup>-2</sup> partial current) was achieved under a small overpotential of 640 mV, which is higher than the performances reported in the literature. With insights from ab initio modelling, we postulate that the locally confined O<sub>2</sub> gas could shift the \*OH binding on various carbon sites in the direction of improved H<sub>2</sub>O<sub>2</sub> activity, through a decrease in solvation energies or a decrease in the \*O coverage around catalytic sites. This local gas confinement approach was successfully extended to other OER-exclusive catalysts, such as nickel metal, for partial H<sub>2</sub>O<sub>2</sub> generation, suggesting its wide applicability.

## Results

**Electrocatalytic 2e<sup>-</sup>-WOR.** We first selected a flat carbon surface to evaluate the relationship between O<sub>2</sub> gas confinement and H<sub>2</sub>O<sub>2</sub> selectivity. Polytetrafluoroethylene (PTFE) polymer islands were deposited onto mirror-polished glassy carbon (GC) electrodes to artificially create an aerophilic surface in aqueous solutions (Fig. 1a and Methods)<sup>29</sup> using a shadow mask-assisted spray-coated method. When a fixed positive potential higher than the onset of OER was applied, the PTFE islands could function as aerophilic centres around which the generated O<sub>2</sub> gas are confined to form gas-liquid-solid triple-phase boundaries (Fig. 1a). Those locally confined O<sub>2</sub> bubbles may in turn interact with the catalytic sites and thus affect the H<sub>2</sub>O<sub>2</sub> selectivity. With O<sub>2</sub> gas continuously produced, the bubbles will gradually grow and eventually leave the surface when the buoyant force becomes larger than the bubble adhesive force on the catalytic surface. Therefore, under steady-state O<sub>2</sub> evolution, the adhesive force of O<sub>2</sub> bubbles could represent the ability of the catalyst to confine local O<sub>2</sub> gas. By tuning the size of the PTFE patterning via a shadow mask-assisted spray coating method (Supplementary Fig. 1 and Methods), we can change the adhesive force of O<sub>2</sub> bubbles on the GC surface and examine the resulting H<sub>2</sub>O<sub>2</sub> selectivity.

A positive potential of 2.05 V versus the reversible hydrogen electrode (RHE) was applied on three different samples as shown in Fig. 1b–g: pristine GC, GC with 300-μm (300-GC) and 200-μm (200-GC) PTFE patterning. While no obvious O<sub>2</sub> bubbles were observed on the surface of pristine GC, PTFE islands were able to accumulate the in situ formed O<sub>2</sub> during the water oxidation process<sup>30</sup> (Fig. 1b and Supplementary Videos 1–3). This is consistent with the different adhesive forces on different surfaces. The pristine GC demonstrates a 21.3-μN adhesive force for an O<sub>2</sub> bubble with an under-electrolyte bubble contact of 156.4° ± 1.6° (Fig. 1h). In sharp contrast, 300-GC and 200-GC offer a much stronger adhesive force of 80.7 and 106.0 μN, respectively, leading to stronger confinements of local gaseous O<sub>2</sub>. Consistently, the under-electrolyte O<sub>2</sub> bubble contact angles of 300-GC and 200-GC (inset of Fig. 1h) decrease to 143.0° ± 0.8° and 118.0° ± 2.1°, respectively, indicating the enhanced aerophilicity of the catalytic surfaces. The different local O<sub>2</sub> confinements result in different H<sub>2</sub>O<sub>2</sub> activities and selectivity. The pristine GC presents an intrinsic H<sub>2</sub>O<sub>2</sub> selectivity of 7.3% on carbon materials, which was gradually improved to 9.0% on 300-GC and further to 11.4% on 200-GC with similar trends to the adhesive force (Fig. 1i). This phenomenon reveals to us that the intrinsic H<sub>2</sub>O<sub>2</sub> selectivity of carbon catalyst could be positively affected by the strength of local O<sub>2</sub> confinement.

To elaborate the possible reaction mechanisms and to further amplify the O<sub>2</sub> confinement effect for improved H<sub>2</sub>O<sub>2</sub> generation performance, a systematic control of the loading of PTFE polymer coating on a three-dimensional porous carbon fibre paper (CFP) electrode was investigated. The polymer loading can be precisely controlled by changing the concentration of PTFE solution during the dip-coating process, where the 5% (CFP-5%), 20% (CFP-20%) and 60% (CFP-60%) PTFE solutions result in a PTFE mass loading (compared to that of CFP) of 12%, 55% and 150%, respectively (Methods). Scanning electron microscopy analysis suggests that PTFE nanoflakes can be uniformly deposited on the surfaces of carbon fibres (Supplementary Fig. 2a,b), providing sufficient triple-phase boundaries and gas confinement for two-electron water oxidation. As expected, the gas adhesive force gradually increased with increased PTFE coating, with consistently decreased under-electrolyte O<sub>2</sub> and increased in-air water contact angles (Supplementary Fig. 3), which we suggest have a direct impact on the water oxidation catalytic activity and selectivity. First, since the PTFE coating repels water and leads to a lower electrochemical surface area (ECSA, Supplementary Fig. 4), the overall geometric current densities were gradually decreased compared to pristine CFP (Fig. 2a). However, the H<sub>2</sub>O<sub>2</sub> selectivity showed a monotonic enhancement with increased PTFE coating (Fig. 2b). The peak H<sub>2</sub>O<sub>2</sub> Faradaic efficiency (FE) of pristine CFP was approximately 10%, but increased to 23%, 31% and 66% in the CFP-5%, CFP-20% and CFP-60% samples, respectively, which represents a maximal sixfold enhancement in H<sub>2</sub>O<sub>2</sub> selectivity (Supplementary Figs. 5 and 6). A similar trend was also observed in other electrolytes such as 1.0 M K<sub>3</sub>PO<sub>4</sub> (pH = 13.18; Supplementary Fig. 7a). We employed gas chromatography to quantify the FEs of gas products during water oxidation. Combining the gas chromatography and H<sub>2</sub>O<sub>2</sub> titration results, we got an overall FE of approximately 100% from the H<sub>2</sub>O-to-O<sub>2</sub> and H<sub>2</sub>O-to-H<sub>2</sub>O<sub>2</sub> processes (Supplementary Fig. 7b) with negligible CO or CO<sub>2</sub> from possible carbon oxidation (lower than the detection limit of the thermal conductivity detector), suggesting that the measured electrocatalytic anodic current exclusively stems from WORs and the CFP is stable under our operating conditions. In addition, no obvious morphology evolution could be observed for PTFE-modified CFP catalyst after electrochemical measurements (Supplementary Fig. 2c,d). The H<sub>2</sub>O<sub>2</sub> evolution onset potential (defined as the potential where the H<sub>2</sub>O<sub>2</sub> concentration reaches 1 ppm after 10 min of electrolysis) of the CFP-60% sample was measured to be only 290 mV, which is among the best compared to previous catalysts<sup>13,14</sup>. More importantly, in contrast to previous oxide catalysts that require large positive potentials (>3 V versus RHE) to deliver H<sub>2</sub>O<sub>2</sub> current densities of approximately 10 mA cm<sup>-2</sup>, the H<sub>2</sub>O-to-H<sub>2</sub>O<sub>2</sub> partial current on our CFP-60% catalyst ramps up quickly to 75.2 mA cm<sup>-2</sup> (23.4 μmol min<sup>-1</sup> cm<sup>-2</sup>) with a maximal 66% selectivity under only 2.4 V versus RHE potential, which represents a high performance compared to existing catalysts (Fig. 2c).

We performed detailed experimental analysis to investigate the possible mechanism for this shift of the water oxidation pathway from 4e<sup>-</sup> to 2e<sup>-</sup>. First, to exclude possible contributions from O<sub>2</sub> plasma treatment, argon annealing or the fluorine dopant during the sample preparation processes, in one control we only treated the pristine CFP using O<sub>2</sub> plasma; in a second we annealed the pristine CFP at 350 °C; in a third we converted the CFP-60% sample into fluorine-doped carbon/CFP by high-temperature annealing in argon atmosphere (Supplementary Fig. 2e,f). The three control electrodes demonstrate similar two-electron water oxidation performances to pristine CFP, with a maximal H<sub>2</sub>O<sub>2</sub> FE of 14.6%, 13.4% and 11.3%, respectively (Supplementary Fig. 7c,d). Second, to demonstrate that the carbon site selectivity for H<sub>2</sub>O<sub>2</sub> formation is not related to the specific surface deposited materials, trimethoxy (1H,1H,2H,

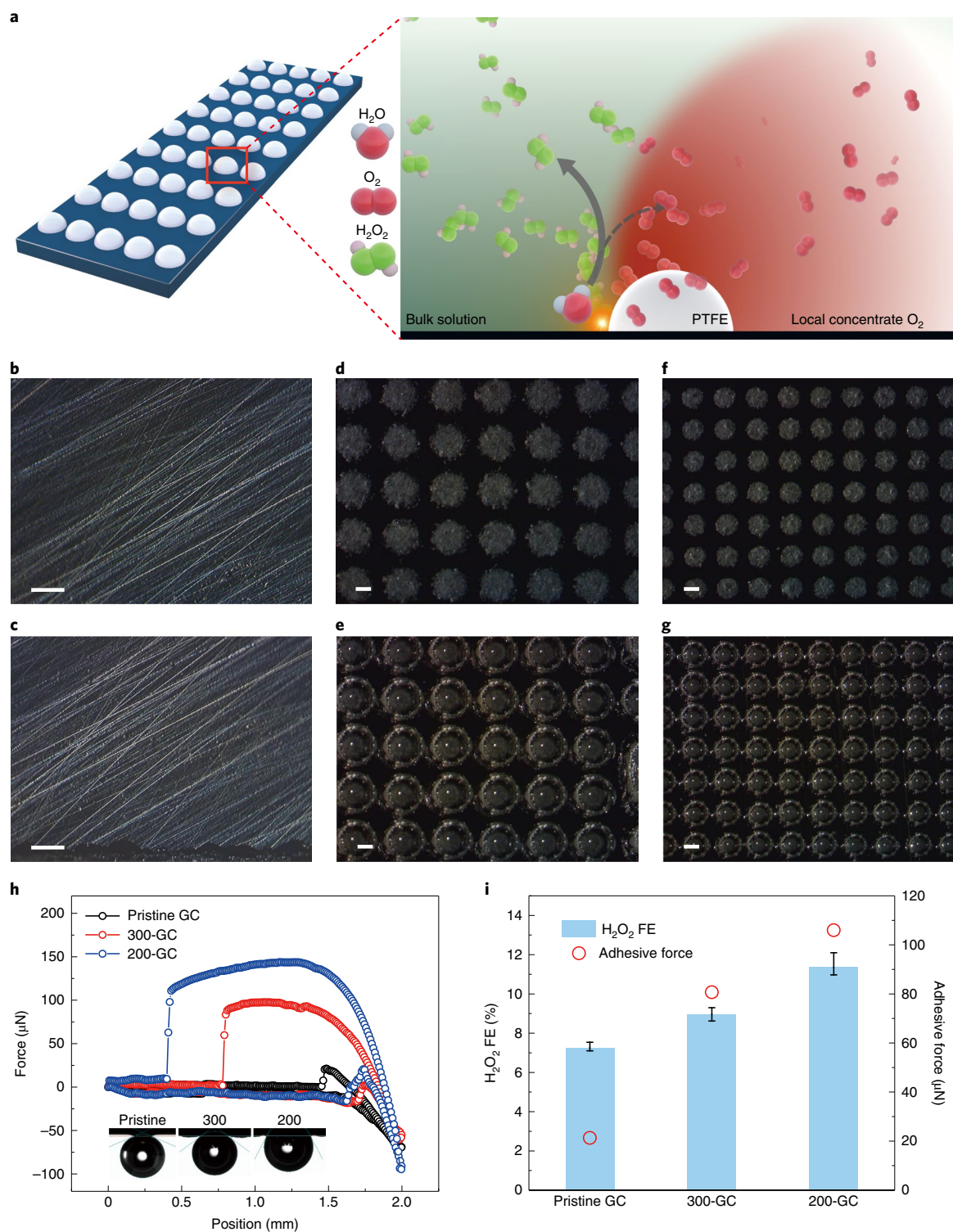


**Fig. 1 | Experimental observation of local product concentration effect.** **a**, A schematic showing the assumed possible reaction pathway tuning by local concentrate product. **b–g**, Digital photos for pristine and PTFE-patterned GC in 1.0 M  $\text{Na}_2\text{CO}_3$  electrolyte: pristine GC recorded at open circuit (**b**) and 2.05 V versus RHE (**c**); 300-GC recorded at open circuit (**d**) and 2.05 V versus RHE (**e**); and 200-GC recorded at open circuit (**f**) and 2.05 V versus RHE (**g**). It is demonstrated that the pristine GC cannot hold any  $\text{O}_2$  bubble on its surface; however, the PTFE-patterned GC is able to concentrate the gaseous  $\text{O}_2$  around the catalytic surface. Scale bars, 300  $\mu\text{m}$ . **h**,  $\text{O}_2$  gas bubble adhesive force measurements for pristine GC, 300-GC and 200-GC electrodes, demonstrating enhanced  $\text{O}_2$  adhesive force of the GC surface after PTFE loading. The insets show the  $\text{O}_2$  bubble contact angles under electrolyte. **i**, The  $\text{H}_2\text{O}_2$  FE of pristine GC, 300-GC and 200-GC catalysts in 1.0 M  $\text{Na}_2\text{CO}_3$  electrolyte at 2.05 V versus RHE, where a monotonic increase of  $\text{H}_2\text{O}_2$  FE was observed with increasing  $\text{O}_2$  bubble adhesive force. The applied potential of GC should be less than 2.1 V versus RHE to prevent GC electrode damage by oxidation during long operation<sup>56</sup>. Thus, 2.05 V versus RHE was chosen for water oxidation measurements. The error bars represent the range of values for three independent samples.

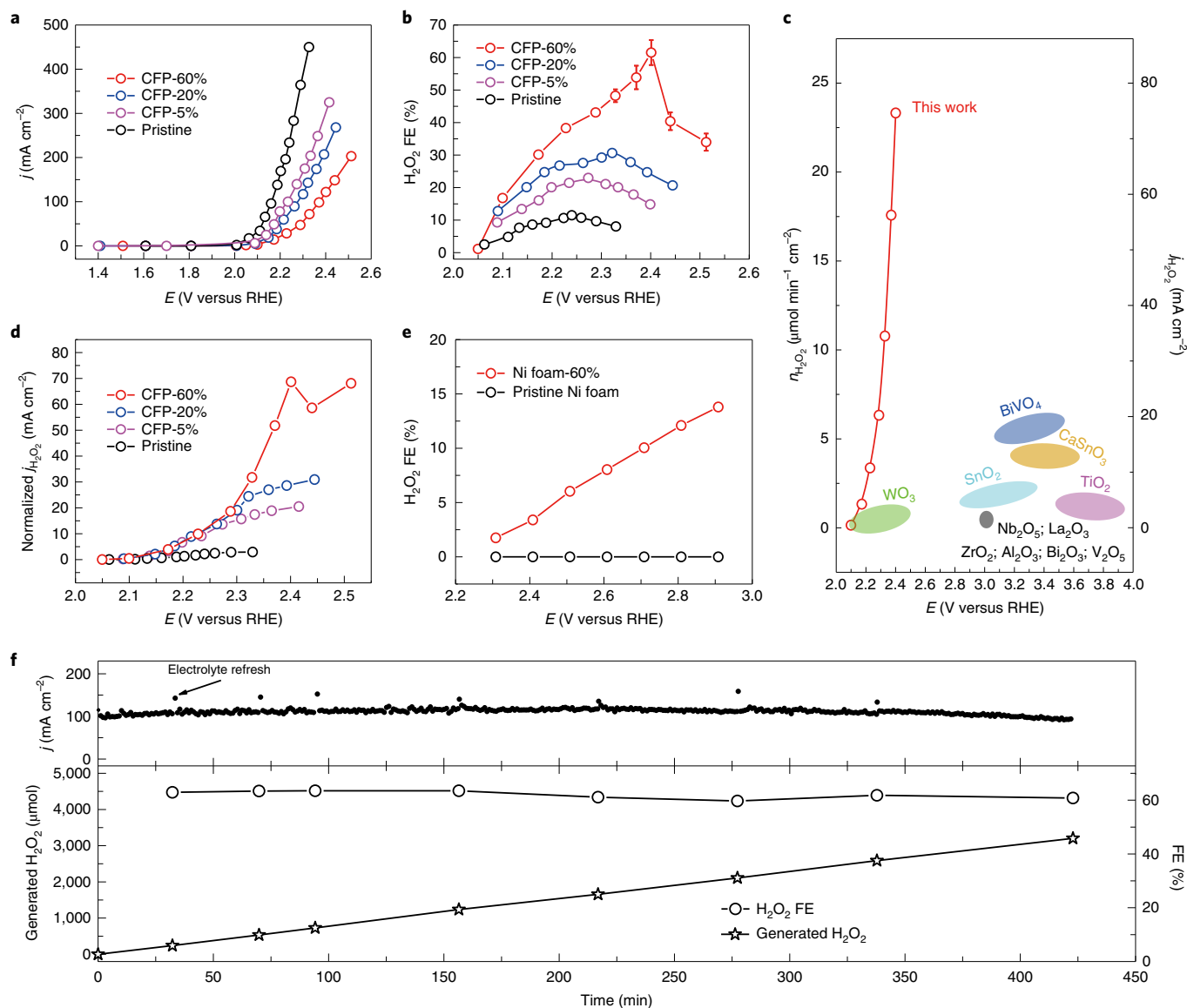


**Fig. 2 | Water oxidation performances on CFP and Ni-based catalysts in 1.0 M  $\text{Na}_2\text{CO}_3$ , pH 11.96.** **a**, The overall current densities of the pristine CFP, CFP-5%, CFP-20% and CFP-60% catalysts. **b**,  $\text{H}_2\text{O}_2$  FEs on pristine CFP, CFP-5%, CFP-20% and CFP-60% at different applied potentials. The highest FE reaches 66%. The error bars represent the range of values for three independent samples. **c**,  $\text{H}_2\text{O}_2$  generation rates of CFP-60% catalyst under different applied potentials. The typically reported two-electron water oxidation catalysts, including  $\text{BiVO}_4$ ,  $\text{CaSnO}_3$ ,  $\text{WO}_3$ ,  $\text{SnO}_2$ ,  $\text{TiO}_2$ ,  $\text{Nb}_2\text{O}_5$ ,  $\text{La}_2\text{O}_3$ ,  $\text{ZrO}_2$ ,  $\text{Al}_2\text{O}_3$ ,  $\text{Bi}_2\text{O}_3$  and  $\text{V}_2\text{O}_5$  (refs. <sup>13,18,27</sup>), are also listed for comparison. **d**, ECSA-normalized  $\text{H}_2\text{O}_2$  production partial current density versus the potential on pristine CFP, CFP-5%, CFP-20% and CFP-60%. **e**,  $\text{H}_2\text{O}_2$  FEs on pristine Ni foam and Ni foam modified with 60% PTFE solution (Ni foam-60%). Note that the potentials for the Ni-based electrode are not  $iR$ -compensated. **f**, The overall current density and  $\text{H}_2\text{O}_2$  FE of CFP-60% catalyst at 2.4 V versus RHE over the course of continuous electrolysis. The geometric area of the CFP-60% electrode is  $0.36 \text{ cm}^2$ .

2H-heptadecafluorodecyl) silane was used to replace the PTFE to create a similar aerophilic surface to trap  $\text{O}_2$  gas<sup>31</sup> (Supplementary Fig. 7e,f). After silane modification, we found that the  $\text{H}_2\text{O}_2$  selectivity of CFP can also be significantly boosted, demonstrating that the confined  $\text{O}_2$  plays a role in promoting  $\text{H}_2\text{O}_2$  selectivity. The above two pieces of evidence show that the carbon site selectivity is related neither to the fabrication processes nor to the surface deposited materials, but could instead be directly linked to local  $\text{O}_2$  concentration.

One may, at first glance, hypothesize that the locally confined  $\text{O}_2$  gas shifts the  $\text{H}_2\text{O}$ -to- $\text{O}_2$  equilibrium towards its reverse reaction ( $\text{O}_2$ -to- $\text{H}_2\text{O}$ ), which potentially suppresses the  $4e^-$  path and thus as a result increases  $\text{H}_2\text{O}_2$  selectivity. However, this equilibrium factor

can be ruled out by comparing the intrinsic activities of carbon sites with ECSA normalization (Fig. 2d and Supplementary Fig. 4); whereas PTFE-modified CFP catalysts presented higher  $\text{H}_2\text{O}_2$  partial currents (more than an order of magnitude) compared to pristine CFP under different applied potentials, indicating their dramatically improved intrinsic  $\text{H}_2\text{O}$ -to- $\text{H}_2\text{O}_2$  catalytic activities, the intrinsic  $\text{H}_2\text{O}$ -to- $\text{O}_2$  activity was similar compared to that of pristine carbon (Supplementary Fig. 8a). Since the pressure/activity of locally confined  $\text{O}_2$  gas does not directly impact the  $\text{H}_2\text{O}$ -to- $\text{H}_2\text{O}_2$  equilibrium, and on the other hand the  $4e^-$  OER equilibrium was not obviously inhibited, we conclude that the enhanced  $\text{H}_2\text{O}_2$  generation performances in our carbon catalyst systems are not due to the simple chemical equilibrium shift effect. We also note that

the different PTFE-coated CFP samples showed quite similar  $\text{H}_2\text{O}_2$  intrinsic activities within a certain potential window until they diverged at large overpotentials, where  $\text{O}_2$  bubbles evolve violently, which further supports our hypothesis that increased confinement of  $\text{O}_2$  gas at the interface has a positive correlation with  $\text{H}_2\text{O}_2$  activity. Furthermore, similar  $\text{H}_2\text{O}$ -to- $\text{H}_2\text{O}_2$  performance was obtained using pristine CFP catalyst in Ar, air and  $\text{O}_2$ -saturated electrolyte (Supplementary Fig. 8b), eliminating the possible contributions from dissolved  $\text{O}_2$  in the electrolyte. These results, taken together, suggest that the locally accumulated  $\text{O}_2$  gas molecules may directly interact with carbon active sites or reaction intermediates, which as a result significantly shifts the water oxidation pathway from  $4e^-$  of  $\text{O}_2$  to  $2e^-$  of  $\text{H}_2\text{O}_2$ .

We found that this concept of confining local  $\text{O}_2$  gas to control the selectivity towards  $\text{H}_2\text{O}_2$  can be successfully extended to other catalytic materials beyond carbon. As an example, we investigated Ni metal foam, which has been established as a highly active, OER-exclusive catalyst<sup>32,33</sup>. As shown in Fig. 2e, we confirmed that while pristine Ni foam did not generate detectable  $\text{H}_2\text{O}_2$ , PTFE-coated Ni foam (Methods) achieves a  $\text{H}_2\text{O}_2$  FE of 13.8% (20 mA  $\text{cm}^{-2}$   $\text{H}_2\text{O}_2$  partial current) at an applied potential of 2.9 V versus RHE.

Finally, as performance stability is a common concern in previously reported  $\text{H}_2\text{O}$ -to- $\text{H}_2\text{O}_2$  catalysts due to their very high overpotentials<sup>34</sup>, we performed chronoamperometry on our CFP-60% catalyst by holding a 2.4 V versus RHE potential where  $\text{H}_2\text{O}_2$  selectivity is maximal (Fig. 2f). The current density showed negligible changes during the course of the stability test. Around 61%  $\text{H}_2\text{O}_2$  selectivity was still maintained after 7 h of continuous electrolysis, demonstrating the good stability of the catalyst over a long operating period (Supplementary Fig. 2c,d). However, we should emphasize here that more work needs to be done to extend the stability from the order of 10 h to thousands of hours for future possible applications. This could be addressed by incorporating other catalytic materials with confined  $\text{O}_2$  effects to further lower the overpotential for high-performance  $\text{H}_2\text{O}_2$  generation.

**Proposed possible mechanisms.** Previous two-electron water oxidation studies on oxide electrocatalysts have suggested an indirect, percarbonate-involved mechanism (Fig. 3a)<sup>13,35,36</sup>. First, the percarbonate species, such as  $\text{HCO}_4^-$  and  $\text{C}_2\text{O}_6^{2-}$ , are generated by electrochemical  $\text{HCO}_3^-$  oxidation on the electrode at a high applied potential. Subsequently, the percarbonate species are hydrolysed by  $\text{H}_2\text{O}$  in the electrolyte, resulting in the formation of  $\text{H}_2\text{O}_2$  and  $\text{HCO}_3^-$ . Based on this mechanism, a significant promotion effect on  $\text{H}_2\text{O}_2$  formation has been observed using bicarbonate electrolyte, for example  $\text{KHCO}_3$  (refs. 13,35). However, in stark contrast to previous reports, the two-electron water oxidation performance of the CFP-60% catalyst in our study is much better in 1.0 M  $\text{Na}_2\text{CO}_3$  electrolyte compared with that in 1.0 M  $\text{NaHCO}_3$  (Supplementary Fig. 9). No promotion effect could be observed using bicarbonate electrolyte in our case, indicating a different mechanism for our carbon catalyst systems. To further explore whether percarbonate intermediates are a possible reaction pathway, we performed oxygen isotope experiments. Isotope ratio mass spectrometry was employed to monitor the  $^{18}\text{O}$  isotope in the samples, which offers an analytical precision ( $1\sigma$ ) of 0.05‰ for  $\delta^{18}\text{O}$  and the values are reported as standard  $\delta$  notation with respect to the Vienna Standard Mean Ocean Water (VSMOW; see Methods)<sup>37</sup>. In our as-obtained  $\text{Na}_2\text{CO}_3$ , the abundance of  $^{18}\text{O}$  is different compared with that in deionized water. The as-obtained  $\text{Na}_2\text{CO}_3$  has a  $\delta^{18}\text{O}$  of 14.99‰. As shown in Fig. 3b, after the fresh preparation of 1.0 M  $\text{Na}_2\text{CO}_3$  solution, we observed a natural isotope oxygen exchange with increased  $\delta^{18}\text{O}$  in  $\text{Na}_2\text{CO}_3$  to 18.33‰ (10 min) and 23.79‰ (2 h). Therefore, within 10 min during which the natural exchange does not reach equilibrium, if the percarbonate is the dominant reaction intermediates, we should be able to observe an  $^{18}\text{O}$  isotope difference between the electrolysed

$\text{Na}_2\text{CO}_3$  and the bare one, considering the violent interaction and chemical bond reconfiguration between the  $\text{HCO}_4^-$  intermediate and  $\text{H}_2\text{O}$  (Fig. 3a). After electrolysis with the passing of 200 C (~10 min), 1 ml of the electrolysed 1.0 M  $\text{Na}_2\text{CO}_3$  solution was taken out; meanwhile another 1 ml of solution was taken from the unelectrolysed bulk 1.0 M  $\text{Na}_2\text{CO}_3$  solution. Then both of the sample solutions were quickly dried in a surface dish at 100 °C. Of note, the natural exchange time with the deionized water was the same for the unelectrolysed and electrolysed  $\text{Na}_2\text{CO}_3$ . As shown in Fig. 3c, the  $\delta^{18}\text{O}$  value for 1.0 M  $\text{Na}_2\text{CO}_3$  electrolyte with and without applied potential showed negligible change (18.31‰ versus 18.33‰). This unchanged  $^{18}\text{O}$  abundance in  $\text{Na}_2\text{CO}_3$  after electrolysis implies that our catalyst systems do not follow the indirect mechanism. It is most likely that the electrocatalytic formation of  $\text{H}_2\text{O}_2$  using our carbon catalysts follows the direct pathway (Fig. 3a).

The complexity of carbon materials, together with the multi-scale nature of the confined  $\text{O}_2$  gas effect observed here, makes it challenging to derive fully converged mechanistic explanations. Instead, we at this point present an ab initio thermodynamic analysis of the complex interface and assess its qualitative contributions to the  $\text{H}_2\text{O}_2$  product selectivity. We hope that these very initial discussions could evolve into more detailed discussions in the future. Carbon materials including both GC and CFP are complex agglomerates of graphene-like structures, and give rise to a wide range of site motifs<sup>38</sup>; the experimentally observed catalytic activity can therefore arise from a variety of active sites<sup>10,39</sup>. For various water oxidation to  $\text{H}_2\text{O}_2$  catalysts, theoretical onset potentials based on binding free energies of  $^*\text{OH}$  ( $\Delta G_{\text{OH}}$ ) have shown a good correlation with experiments, suggesting that  $\Delta G_{\text{OH}}$  is a meaningful descriptor<sup>13</sup>. In the present work, we thus consider the  $^*\text{OH}$  binding energies at various coverages on four structures of defected graphene (O-basal 1, O-basal 2, OH-basal and 5555-6-7777 defective), all of which have been shown to weakly bind  $\text{OH}^*$  and are therefore expected to be relevant active sites in the range of water oxidation to  $\text{H}_2\text{O}_2$  (refs. 10,39), as well as partially and fully oxidized graphene (Methods; Supplementary Fig. 1e).

Figure 3 shows the volcano plots for  $2e^-$  water oxidation for the considered structures as a function of  $\Delta G_{\text{OH}}$ . The active site models used in this work span a wide range of catalytic activities on both sides of the volcano. We postulate here that slight modulations of the  $^*\text{OH}$  binding energy, arising from those trapped  $\text{O}_2$  gas bubbles, can lead to significant improvements in  $\text{H}_2\text{O}_2$  activity and selectivity.

Two possible effects of the  $\text{O}_2$  gas bubbles are as follows. First, the solvation stabilization may be decreased, since the presence of  $\text{O}_2$  gas molecules interrupts hydrogen bonding networks and therefore reduces the average number of possible hydrogen bonds<sup>40</sup>. In aqueous solution, it has been experimentally and theoretically reported that adsorbed  $^*\text{OH}$  is stabilized by 0.4–0.8 eV by hydrogen bonding interactions with nearby  $\text{H}_2\text{O}$  molecules<sup>41–43</sup>. By using a combined explicit and implicit solvation approach<sup>44</sup>, we found a solvation stabilization effect of up to around 0.3 eV (Supplementary Table 1), which lies at the bottom of the previously reported range. Although this value may vary depending on the surface and external conditions, such as potential and pH, we generally expect the  $^*\text{OH}$  binding to be weakened due to missing hydrogen bonding networks, which will shift the less oxidized defected active sites (yellow and light green symbols in Fig. 3d) towards the activity peak of the volcano plot.

Second, the reduced local  $\text{H}_2\text{O}$  concentration near the surface due to the trapped  $\text{O}_2$  bubbles can lead to a decrease of the oxidation of the graphene surfaces, which in turn weakens  $^*\text{OH}$  binding. This was confirmed by operando Raman spectroscopy, in that, under WOR conditions, the CFP-60% showed a less oxidized surface than that of pristine CFP (Supplementary Fig. 10). The strong electrochemical driving force to generate  $^*\text{O}$  coverage from  $\text{H}_2\text{O}$  makes

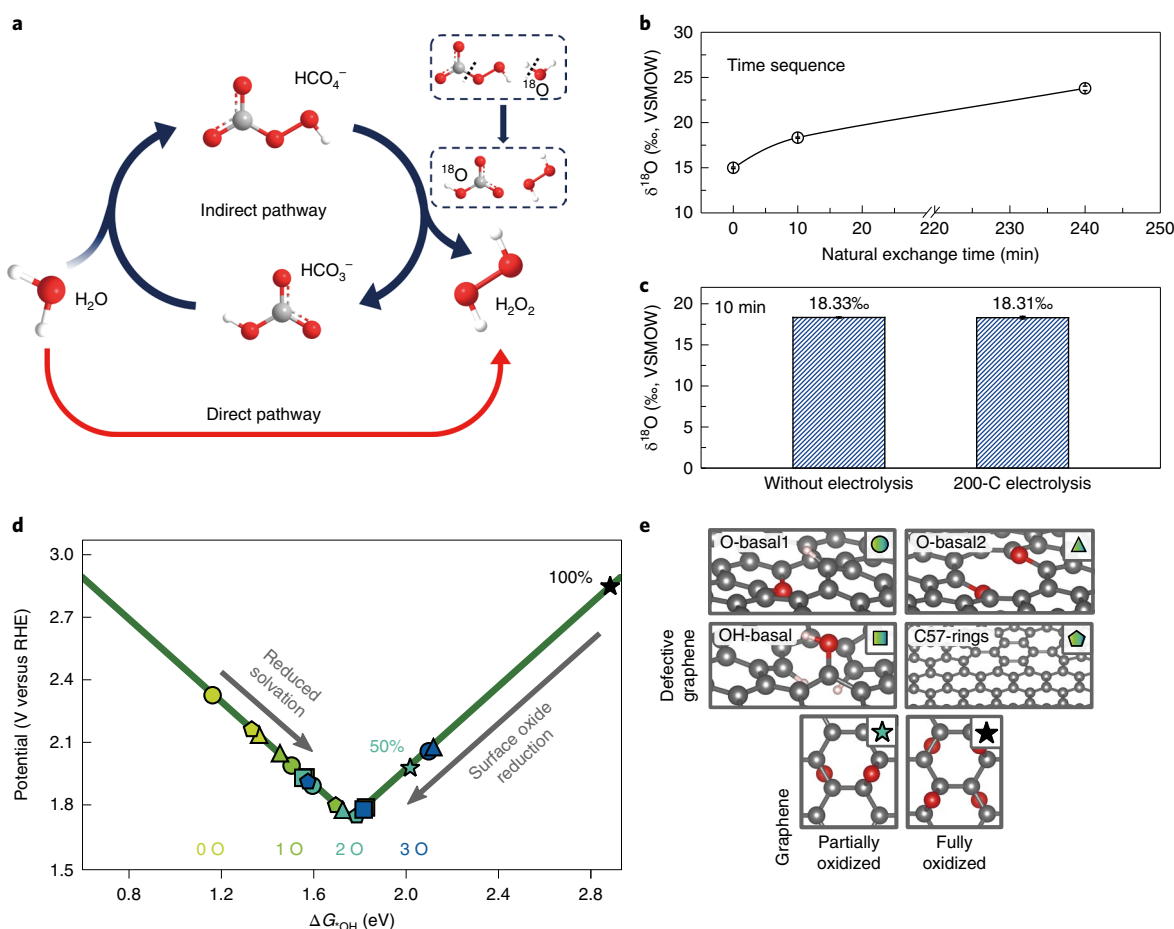


**Fig. 3 | Possible mechanisms.** **a**, Two different reaction pathways for catalytic two-electron water oxidation. **b**,  $^{18}\text{O}$  isotope abundance in quickly dried (within 2 min, Methods) 1.0 M  $\text{Na}_2\text{CO}_3$  electrolyte with varied isotope exchange time between  $\text{Na}_2\text{CO}_3$  solute and deionized water. The analytical precision ( $1\sigma$ ) is 0.05‰ for  $\delta^{18}\text{O}$ , and the values are reported as standard  $\delta$  notation with respect to VSMOW. **c**,  $^{18}\text{O}$  isotope abundance in quickly dried 1.0 M  $\text{Na}_2\text{CO}_3$  electrolyte with or without applied potential (2.4 V versus RHE). The error bars in **b** and **c** represent two independent tests. **d, e**,  $2e^-$  volcano plot of  $\text{H}_2\text{O}$  oxidation as a function of the  $^*\text{OH}$  binding energy ( $\Delta G_{\text{OH}}$ ) (**d**). The data points depict  $^*\text{OH}$  binding energies on defected graphene sheets (circles, pentagons, triangles and squares) as well as partially (50%) and fully oxidized graphene sheets (stars) (without correction for solvation effects) and are schematically drawn (**e**). In the case of the defected structures, four different typical defects were considered as well as different coverages of oxygen atoms in the vicinity of the active site indicated by the yellow (low coverage, no  $^*\text{O}$  in the vicinity, structures shown in **e**) to blue (high coverage, 3  $^*\text{O}$  in the vicinity) colour scale. Arrows indicate potential external driving forces, which probably influence the  $\text{H}_2\text{O}_2$  selectivity by decreasing solvation stabilization due to the creation of water-poor oxygen bubbles or by reducing the degree of surface oxidation.

this process highly sensitive to the water chemical potential. On the other hand,  $\text{O}_2$  chemical dissociation plays only a minor role, even if large  $\text{O}_2$  pressures are present inside the bubbles, because of the relatively small thermochemical driving force compared to water oxidation (Supplementary Fig. 11) and the high  $\text{O}_2$  chemical dissociation barrier ( $>2\text{ eV}$ )<sup>45,46</sup>. It is thus the presence of  $\text{H}_2\text{O}$  molecules under the influence of a high electrochemical potential (2–3 V versus RHE) that leads to a significant oxidation of the carbon material. Our surface Pourbaix analysis (Supplementary Fig. 12 and 13) of all structures shows that it is thermodynamically favourable to completely saturate the surface with oxygen. In the steady state, however, the surface might not be fully oxidized due to significant kinetic barriers for surface to subsurface O diffusion ( $>4\text{ eV}$ )<sup>47</sup>. This leads to free active sites where  $^*\text{OH}$  can bind surrounded by a highly oxidized carbon environment. A high degree of oxidation localizes the  $^*\text{OH}$  binding energy at the right, weak-binding leg of the volcano (Fig. 3d). Consequently, a decrease in the  $\text{H}_2\text{O}$  concentration inside the  $\text{O}_2$  bubbles and the corresponding decrease in surface oxidation would shift such sites to stronger  $^*\text{OH}$  binding and higher  $\text{H}_2\text{O}_2$  activity (Supplementary Fig. 14). Based on

both the experimental and theoretical investigations, we conclude that the specific properties of the PTFE–CFP systems lead to less oxidized surfaces as well as water-poor regions in the created  $\text{O}_2$  bubbles, which could both shift the  $^*\text{OH}$  binding energy of active sites to the top of the volcano thereby improving  $\text{H}_2\text{O}_2$  activity, as summarized in the schematic diagram in Supplementary Fig. 15.

**$\text{H}_2\text{O}_2$  electrosynthetic cell.** This high-performance  $2e^-$ -WOR catalyst, when coupled with an active and selective  $2e^-$ -ORR cathode<sup>9,10</sup>, can enable a highly efficient  $\text{H}_2\text{O}_2$  electrosynthetic cell, where  $\text{H}_2\text{O}_2$  can be selectively generated from both electrodes. In contrast to previous  $4e^-$ -WOR/ $2e^-$ -ORR systems, where the maximal  $\text{H}_2\text{O}_2$  FE of the cell ( $\text{FE}_{\text{cell}}$ ) was defined as 100% (ref. 15), our  $2e^-$ -WOR/ $2e^-$ -ORR system can reach a maximal  $\text{H}_2\text{O}_2$   $\text{FE}_{\text{cell}}$  of 200% (Methods), as two electrons shuttled from anode to cathode can maximally produce two  $\text{H}_2\text{O}_2$  molecules. Here we demonstrate a membrane-free  $\text{H}_2\text{O}_2$  electrocatalytic generation flow cell with a state-of-the-art  $\text{H}_2\text{O}_2$  generation rate and efficiency (Fig. 4a, Methods). The oxidized carbon nanotube<sup>10</sup> was employed as an efficient and stable  $2e^-$ -ORR catalyst (Supplementary Fig. 16) to couple with our

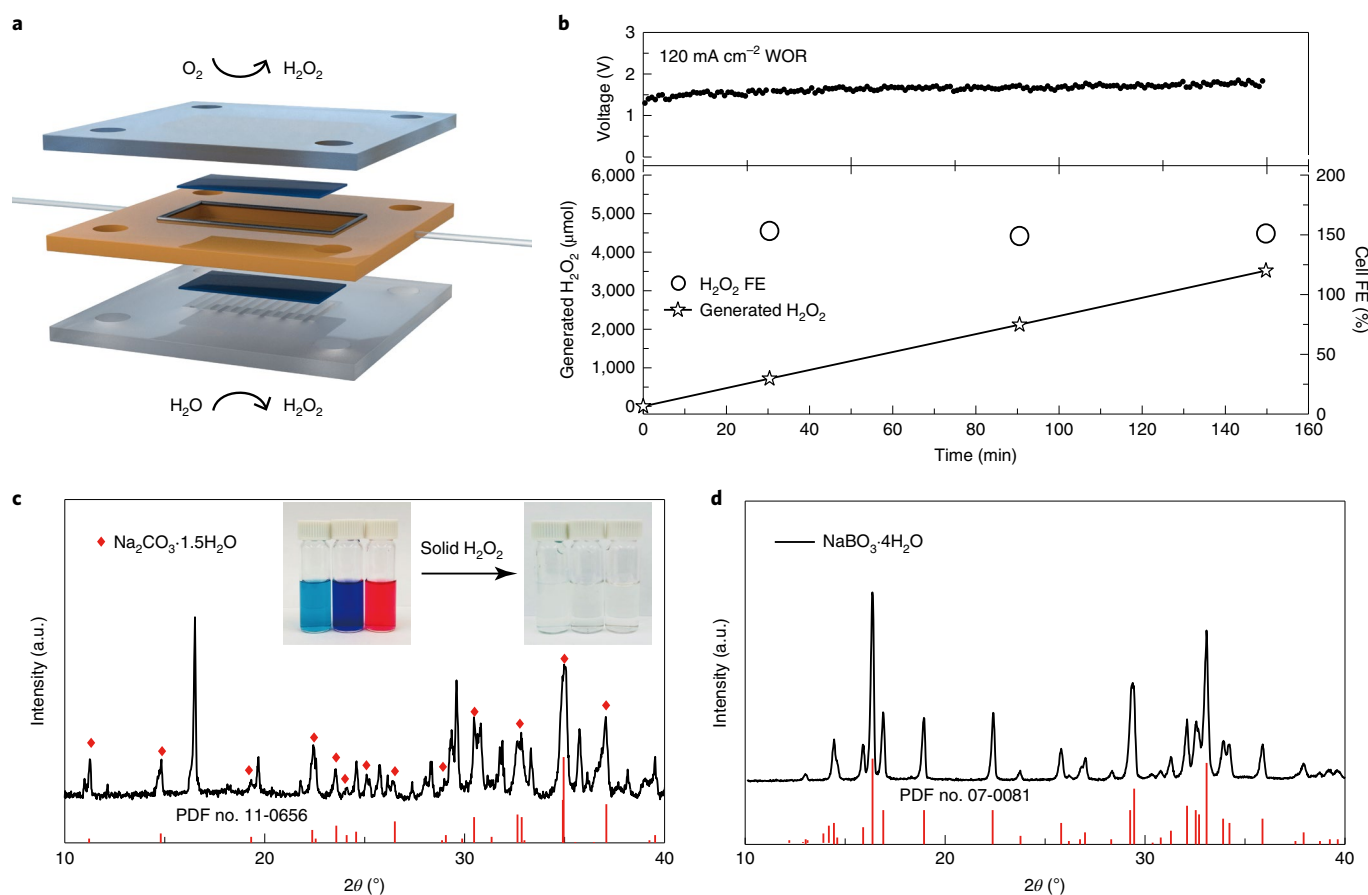


**Fig. 4 | Applications of developed 2e<sup>-</sup>-WOR//2e<sup>-</sup>-ORR H<sub>2</sub>O<sub>2</sub> electrosynthetic cell. **a**, Schematic design of our H<sub>2</sub>O<sub>2</sub> production prototype cell. **b**, H<sub>2</sub>O<sub>2</sub> generation performance of our 2e<sup>-</sup>-ORR//2e<sup>-</sup>-WOR cell, which demonstrates an electricity-to-H<sub>2</sub>O<sub>2</sub> efficiency of 90%, making it highly competitive with traditional anthraquinone oxidation technology. **c**, The XRD pattern for as-extracted solid H<sub>2</sub>O<sub>2</sub> from electrolyte after electrolysis (Na<sub>2</sub>CO<sub>3</sub>+1.5H<sub>2</sub>O<sub>2</sub>→Na<sub>2</sub>CO<sub>3</sub>·1.5H<sub>2</sub>O<sub>2</sub>). The red rhombus symbols represent the peaks that originate from Na<sub>2</sub>CO<sub>3</sub>·1.5H<sub>2</sub>O<sub>2</sub> (PDF no. 11-0656). All other peaks can be ascribed to hydrated Na<sub>2</sub>CO<sub>3</sub> (Na<sub>2</sub>CO<sub>3</sub>·H<sub>2</sub>O and Na<sub>2</sub>CO<sub>3</sub>·7H<sub>2</sub>O). The inset of **c** shows the dye degradation using aged solid H<sub>2</sub>O<sub>2</sub>, which was stored under ambient conditions for 2 months, highlighting the stability and reliability of solid H<sub>2</sub>O<sub>2</sub> compared to liquid H<sub>2</sub>O<sub>2</sub>. The colour image shows the pristine dye solution. The transparent one is the dye solution after reaction with solid H<sub>2</sub>O<sub>2</sub>. **d**, The XRD pattern for as-obtained sodium perborate (Na<sub>2</sub>BO<sub>3</sub>·4H<sub>2</sub>O), demonstrating the successful synthesis of pure high-value-added sodium perborate.**

CFP-60% anode. Only a cell voltage of approximately 1.7 V was required to reach a cell current of 50.4 mA (120 mA cm<sup>-2</sup> WOR) in our 2e<sup>-</sup>-WOR//2e<sup>-</sup>-ORR cell (Fig. 4b and Methods), delivering a H<sub>2</sub>O<sub>2</sub> FE<sub>cell</sub> of 153%. This result agrees well with H<sub>2</sub>O<sub>2</sub> selectivity on WOR (~60%) and ORR (~90%) catalysts when tested individually in a standard three-electrode setup. An impressive H<sub>2</sub>O<sub>2</sub> production rate of 24 μmol min<sup>-1</sup> was achieved in our electrosynthetic cell. This extraordinary current efficiency makes the electrochemical H<sub>2</sub>O<sub>2</sub> synthesis cell highly competitive relative to energy-demanding anthraquinone cycling (Supplementary Note 1). This on-site H<sub>2</sub>O<sub>2</sub> flow generation opens up opportunities in a wide range of practical applications<sup>7</sup>, for example domestic sewage treatment. We showed a representative demonstration here where by feeding the continuously produced H<sub>2</sub>O<sub>2</sub> solution, the organic contamination in water can be rapidly degraded (Supplementary Fig. 17a and Supplementary Video 4). Furthermore, to minimize the transportation and storage cost of liquid H<sub>2</sub>O<sub>2</sub>, solid H<sub>2</sub>O<sub>2</sub> powder—an adduct product between Na<sub>2</sub>CO<sub>3</sub> and H<sub>2</sub>O<sub>2</sub> (Na<sub>2</sub>CO<sub>3</sub>·1.5H<sub>2</sub>O<sub>2</sub>)<sup>48</sup>—was directly extracted from the Na<sub>2</sub>CO<sub>3</sub> electrolyte after a continuous electrolysis (Supplementary Fig. 17b and Methods). Both X-ray diffraction (XRD) and X-ray photoelectron spectroscopy (XPS) analysis (Fig. 4c and Supplementary Fig. 18) confirmed the successful preparation of solid H<sub>2</sub>O<sub>2</sub>, which is more stable and reliable

than liquid H<sub>2</sub>O<sub>2</sub> (ref. 49). We showed that the solid H<sub>2</sub>O<sub>2</sub> powders were still highly active for organic dye degradation after 2 months storage under ambient conditions (Fig. 4c and Supplementary Video 5). Meanwhile, we demonstrated that other high-value products, for example sodium perborate (Fig. 4d), can be generated in situ and precipitated out by simply adding sodium metaborate into the electrolyte.

## Conclusions

Taken together, our experimental and theoretical results demonstrate the efficacy of our catalyst design concept, that accumulated local gaseous O<sub>2</sub> can shift the energetics of the WOR in favour of 2e<sup>-</sup> of H<sub>2</sub>O<sub>2</sub> generation. From experiments and density functional theory studies, we explain this shift by the generation of a triple-phase boundary at which the \*OH binding energy shifts towards the top of the volcano by a less oxidized reaction environment and missing hydrogen bonding to surrounding water. Future studies will be directed towards more uniform and stable coating of hydrophobic materials to further boost the local O<sub>2</sub> concentration and prevent wetting after long-term operation. Additionally, our investigations into Ni suggest that higher activity and selectivity can be achieved by applying this concept on known H<sub>2</sub>O-to-H<sub>2</sub>O<sub>2</sub> catalysts. Fine characterizations on crystalline catalysts will further allow

computational simulations to study in detail the mechanism and the origin of the improvement in the catalytic performance.

## Methods

**Preparation of PTFE-patterned GC.** The shadow mask patterns are designed from CircuitMaster software. Polyimide substrate was pinned through a vacuum environment and LPFK Protolaser U3 (focal length,  $f=103$  mm, wavelength,  $\lambda=355$  nm) was used to fabricate the polyimide shadow mask through direct laser engraving. Then, 1 ml of 60% PTFE aqueous solution (Sigma) was spray-coated onto the GC (HTW) surface with the help of the polyimide shadow mask to obtain the well-defined PTFE patterns. After drying at 120 °C under ambient conditions, the PTFE-patterned GC samples were annealed at 350 °C under argon atmosphere for 30 min to obtain a superaerophilic surface to accumulate the locally produced O<sub>2</sub>.

**Preparation of PTFE-decorated CFP.** To create a hydrophilic surface, 190- $\mu$ m-thick CFP (Fuel Cell Store) was pretreated by oxygen plasma (50 W, 2 min). Then, 2  $\times$  5 cm<sup>2</sup> as-treated CFP was soaked into 60% (5% or 20%) PTFE aqueous solution for 10 min and then dried at 120 °C under ambient conditions. Note that the 5% and 20% PTFE solutions were diluted from 60% PTFE. Next, the PTFE-loaded CFP samples were annealed at 350 °C under argon atmosphere for 30 min to obtain a superaerophilic surface to accumulate the locally produced O<sub>2</sub>. The mass loadings of PTFE (the mass different before and after surface modification) for CFP-5%, CFP-20% and CFP-60% were approximately 12%, 55% and 150%, respectively.

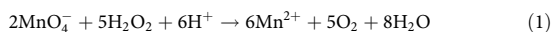
**Preparation of FAS-decorated CFP.** To introduce hydrophilic functional groups, 190- $\mu$ m-thick CFP was pretreated with oxygen plasma (50 W, 10 min). Then, trimethoxy (1H,1H,2H,2H-heptadecafluorodecyl) silane (FAS) was used as the chemical vapour deposition material to increase the gas adhesive force of CFP, which was carried out in a beaker that contained FAS/ethanol solution (80  $\mu$ l:4 ml in volume) in equilibrium with its vapour. The plasma-treated electrode was exposed to FAS vapour for 30 h under ambient conditions to create an aerophilic CFP-FAS electrode.

**Preparation of control samples.** The O<sub>2</sub> plasma-treated CFP sample was prepared by 50 W oxygen plasma functionalization for 2 min. The pristine CFP was calcinated at 350 °C under argon atmosphere for 30 min to obtain the argon annealed sample. The CFP-60% electrode was annealed at 900 °C under argon atmosphere for 1 h to fabricate the fluorine-doped carbon/CFP electrode.

**Preparation of oxidized carbon material for oxygen reduction.** The oxidized carbon nanotube was prepared according to a previous report<sup>10</sup>.

**Electrocatalytic oxidation of H<sub>2</sub>O.** The electrochemical measurements were run at 25 °C in a customized gas-tight H-type glass cell separated by Nafion 117 membrane (Fuel Cell Store). A BioLogic VMP3 workstation was employed to record the electrochemical response. In a typical three-electrode system, a platinum foil (Beantown Chemical, 99.99%) and a saturated calomel electrode (SCE, CH Instruments) were used as the counter and reference electrode, respectively. The carbon electrodes (pristine and PTFE-patterned GC; pristine and PTFE-decorated CFP; ~1 cm<sup>2</sup>) were used as the working electrodes. The rear side of the GC was covered by an electrochemically inert, hydrophobic wax (Apiezon wax WW100) during electrochemical tests. Before electrochemical measurements, all samples were prestabilized at 1.2 V versus SCE to achieve a stable current density in the 1.0 M Na<sub>2</sub>CO<sub>3</sub> electrolyte. All potentials measured against SCE ( $E_{\text{SCE}}$ ) were converted to the RHE ( $E_{\text{RHE}}$ ) scale in this work using  $E_{\text{RHE}} = E_{\text{SCE}} \times 0.244 \text{ V} + 0.0591 \times \text{pH}$ , where pH values of the electrolytes were determined by an Orion 320 PerpHecT LogR Meter (Thermo Scientific). In this study, 1.0 M Na<sub>2</sub>CO<sub>3</sub> aqueous solution was used as the electrolyte with a pH of 11.96. Note that 4 mg ml<sup>-1</sup> Na<sub>2</sub>SiO<sub>3</sub> (Sigma) was added into the electrolyte to stabilize the H<sub>2</sub>O<sub>2</sub> formed during stability measurements. The electrolyte in the anodic compartment was stirred at a rate of 1,000 r.p.m. during electrolysis. Solution resistance was determined by potentiostatic electrochemical impedance spectroscopy at frequencies ranging from 0.1 Hz to 200 kHz. All the measured potentials were manually compensated unless stated otherwise.

After electrolysis with the passing of ~10–50 C, the generated H<sub>2</sub>O<sub>2</sub> concentration was first roughly detected by using standard H<sub>2</sub>O<sub>2</sub> strips (Indigo Instruments), and further confirmed using the standard potassium permanganate (0.1 N KMnO<sub>4</sub> solution, Sigma-Aldrich) titration process, according to the following equation:



In this work, sulfuric acid (2.0 N H<sub>2</sub>SO<sub>4</sub>, VWR International Company) was used as the H<sup>+</sup> source. The FE for H<sub>2</sub>O<sub>2</sub> production is calculated using the following equation:

$$\text{FE} = \frac{\text{generated H}_2\text{O}_2 \text{ (mol)} \times 2 \times 96,485}{\text{total amount of charge passed (C)}} \times 100 \text{ (maximum 100\%)} \quad (2)$$

To quantify the gas products during electrolysis, argon gas (Airgas, 99.995%) was delivered into the anodic compartment at a rate of 20.0 standard cubic centimetres per minute (sccm, monitored by an Alicat Scientific mass flow controller) and vented into a gas chromatograph (Shimadzu gas chromatography-2014) equipped with a combination of molecular sieve 5 Å, Hayesep Q, Hayesep T and Hayesep N columns. A thermal conductivity detector was mainly used to quantify gas product concentration. The partial current density for the O<sub>2</sub> produced was calculated as follows:

$$j_i = x_i \times v \times \frac{n_i F p^0}{RT} \times (\text{electrode area})^{-1} \quad (3)$$

where  $x_i$  is the volume fraction of the certain product determined by online gas chromatography referenced to calibration curves from the standard gas sample (Airgas),  $v$  is the flow rate of 20 sccm,  $n_i$  is the number of electrons involved,  $p^0 = 101.3$  kPa,  $F$  is the Faradaic constant,  $T = 298$  K and  $R$  is the gas constant. The corresponding FE at each potential is calculated as  $\frac{j_i}{j_{\text{overall}}} \times 100$ .

For the 2e<sup>-</sup>-WOR//2e<sup>-</sup>-ORR electrocatalytic cell test, 0.5 mg cm<sup>-2</sup> oxidized carbon nanotube catalyst was air-brushed onto 2-cm<sup>2</sup> Sigracet 35 BC gas diffusion layer (Fuel Cell Store) electrodes as 2e<sup>-</sup>-ORR cathode. Then, a 0.42-cm<sup>2</sup> CFP-60% electrode was used as anode. The two electrodes were therefore placed on opposite sides in the flow cell<sup>49</sup> without a separation membrane. O<sub>2</sub>-saturated 1.0 M Na<sub>2</sub>CO<sub>3</sub> with 4 mg ml<sup>-1</sup> Na<sub>2</sub>SiO<sub>3</sub> was used as electrolyte. The cathode was open to the atmosphere. The flow rate of 1.0 M Na<sub>2</sub>CO<sub>3</sub> electrolyte was 5 ml min<sup>-1</sup>, as controlled by a peristaltic pump. A current of 50.4 mA was employed for H<sub>2</sub>O<sub>2</sub> production. To extract the solid H<sub>2</sub>O<sub>2</sub> from the electrolyte after electrolysis (three-electrode configuration, 25 ml 1.0 M Na<sub>2</sub>CO<sub>3</sub> electrolyte, electrolysis at 2.4 V versus RHE at 5 °C for 5 d; the CFP-60% catalyst was replaced using fresh catalyst after every 24 h; Bipolar membrane (Fuel Cell Store) was used to replace the Nafion 117; the cathode was coupled with two-electron ORR using oxidized carbon nanotube electrode), about 100 ml of absolute ethanol is added into 20 ml of the electrolyte, and the mixture is mechanically stirred. The precipitate is isolated by vacuum filtration and washed several times with absolute ethanol. The isolated precipitate is then dried in a vacuum oven at room temperature for 24 h. For sodium perborate synthesis, a solution containing of 2.0 M NaBO<sub>2</sub> and 1.0 M Na<sub>2</sub>CO<sub>3</sub> was used as electrolyte. The electrolysis was performed at a current density of 120 mA cm<sup>-2</sup> at 5 °C. The white precipitate (sodium perborate) that was formed in situ during electrolysis was collected for further characterization.

The FE of the electrocatalytic cell for H<sub>2</sub>O<sub>2</sub> production and the corresponding electricity-to-H<sub>2</sub>O<sub>2</sub> efficiency are calculated using the following equations, respectively:

$$\text{FE}_{\text{cell}} = \frac{\text{generated H}_2\text{O}_2 \text{ (mol)} \times 2 \times 96,485}{\text{total amount of charge passed (C)}} \times 100 \text{ (maximum 200\%)} \quad (4)$$

$$\text{Electricity to H}_2\text{O}_2 \text{ efficiency} = \frac{E_{2e^--\text{WOR}} - E_{2e^--\text{ORR}}}{E_{\text{cell}}} \times \text{FE}_{\text{cell}} \text{ (maximum 200\%)} \quad (5)$$

where  $E_{2e^--\text{WOR}}$  (1.76 V)<sup>13</sup> and  $E_{2e^--\text{ORR}}$  (0.76 V)<sup>11</sup> are the theoretical potential for two-electron water oxidation and two-electron oxygen reduction, respectively.  $E_{\text{cell}}$  is the required cell voltage to offer a current density of 120 mA cm<sup>-2</sup>.

**Characterization.** Powder XRD data were collected using a Bruker D2 Phaser diffractometer in parallel beam geometry employing Cu K $\alpha$  radiation ( $\lambda = 1.54056$  Å) and a one-dimensional LYNXEYE detector, at a scan speed of 0.02° per step and a holding time of 1 s per step. XPS was carried out with a Thermo Scientific K-Alpha ESCA spectrometer, using monochromatic Al K $\alpha$  radiation (1486.6 eV) and a low-energy flood gun as neutralizer. All XPS spectra were calibrated by shifting the detected carbon C 1s peak to 284.6 eV. Scanning electron microscopy was performed on a Zeiss Supra55VP field emission scanning electron microscope with in-lens detector. The contact angles of O<sub>2</sub> gas bubbles under electrolyte were tested by the method of captive bubble<sup>50</sup> and the bubble size was controlled at 2  $\mu$ l. Adhesive forces between the O<sub>2</sub> bubbles and electrodes were assessed using DataPhysics DCAT 21.

**<sup>18</sup>O isotope measurement.** First, 0.2 mol (21.2 g) Na<sub>2</sub>CO<sub>3</sub> (Sigma) was dissolved into 200 ml of ultrapure Milli-Q water. After stirring for 5 min, 25 ml of the fresh 1.0 M Na<sub>2</sub>CO<sub>3</sub> solution was used as the electrolyte for water oxidation. After electrolysis with the passing of 200 C, 1 ml of the electrolysed 1.0 M Na<sub>2</sub>CO<sub>3</sub> solution was taken out; meanwhile another 1 ml of solution was taken from the unelectrolysed bulk 1.0 M Na<sub>2</sub>CO<sub>3</sub> solution. Then both of the sample solutions were quickly dried (within 2 min) in a surface dish at 100 °C. Of note, the natural exchange time with the water was the same for the unelectrolysed and electrolysed Na<sub>2</sub>CO<sub>3</sub>. Next, the dried Na<sub>2</sub>CO<sub>3</sub> powder was collected for <sup>18</sup>O isotope analysis. Oxygen isotope analysis was performed on a GasBench-Conflo-Isotope Ratio Mass Spectrometer (Delta V, Thermo Scientific) system. Then ~0.190 mg of sodium carbonate (Na<sub>2</sub>CO<sub>3</sub>) were weighed out into an exetainer, which was flushed by helium flow for 10 min on the GasBench. Then 0.3 ml of 105% phosphoric acid was added into the exetainer for 24-h reaction. The generated CO<sub>2</sub> gas was then

delivered to the mass spectrometry for isotope ratio analysis. The oxygen isotope composition of the carbonate was calculated based on the measured oxygen isotope composition of the CO<sub>2</sub> gas, based on the fractionation factor between the two at the reaction temperature. Oxygen isotope values are reported in a  $\delta$  notation, with respect to the VSMOW international standard.

**Operando Raman measurement.** For operando electrochemical Raman spectroscopy measurements, a piece of CFP (1 cm<sup>2</sup>, with or without PTFE treatment) was first stuck onto a polished GC electrode with a conductive carbon tape and then assembled into a homemade three-electrode spectroelectrochemical cell. The Raman spectra were recorded on a Horiba LabRAM HR 800 confocal Raman microscopy, with the signals excited by a 532-nm Ventus VIS laser and collected by a  $\times 100$  objective, with a dispersion grating of 600 gmm<sup>-1</sup> and a co-adding of 64 scans. A Biological VSP potentiostat was used for potential control.

**ECSA measurement.** The ECSA was determined by measuring the capacitive current associated with double-layer charging from the scan-rate dependence of cyclic voltammetry. Before ECSA measurements, all samples were pre-stabilized at 1.2 V versus SCE to achieve a stable current density in the 1.0 M Na<sub>2</sub>CO<sub>3</sub> electrolyte. By plotting the difference in the current density ( $j$ ) between the anodic and cathodic sweeps ( $\Delta j$ ) at a fixed potential against the scan rate, a linear trend was observed. The fitting slope was twice the double-layer capacitance ( $C_{dl}$ ), which is linearly proportional to the ECSA. These values of  $C_{dl}$  permit the comparison of the relative surface activity of different electrodes, particularly in the same electrolyte. To determine  $C_{dl}$  for various electrodes, the potential window of the cyclic voltammeters was 0.15–0.25 V versus SCE with the scan rates from 50 mV s<sup>-1</sup> to 150 mV s<sup>-1</sup>. Based on our previous work<sup>49</sup>, the double-layer capacitance of the flat GC electrode was measured to be approximately 24  $\mu\text{F cm}^{-2}$ . Thus, this value of 24  $\mu\text{F cm}^{-2}$  was used for ECSA normalization.

**Computational methods.** Density functional theory calculations were performed using the Vienna Ab Initio Simulation Package (VASP)<sup>51,52</sup> with the Bayesian error estimation exchange-correlation functional with van der Waals correction (BEEF-vdW)<sup>53</sup> and projector augmented-wave pseudopotential<sup>54</sup>. The energy cutoff, a convergence criterion for self-consistent iteration and geometry relaxation were set to 500 eV, 10<sup>-4</sup> eV and 0.05 eV  $\text{\AA}^{-1}$ , respectively. To simulate various carbon structures with a wide range of catalytic activities, we modelled four different structures (O-basal 1, O-basal 2, OH-basal and 5555-6-7777 defective) using (6  $\times$  6) graphene, which have been shown to be active for H<sub>2</sub>O oxidation<sup>10,40</sup>. Additionally, we considered partially and fully oxidized graphene using (1  $\times$  2) graphene. We added 15  $\text{\AA}$  of vacuum layer to avoid non-physical interactions between repeating layers in the z direction. For large cells, a gamma point mesh was used, whereas for small oxidized graphene cells, (6  $\times$  5  $\times$  1) meshes were used, which showed a negligible difference compared to (12  $\times$  10  $\times$  1) mesh calculations. To test the effect of the implicit solvation, we used VASPsol with default parameter settings and a dielectric constant set to that of water ( $\epsilon = 78.4$ )<sup>45</sup>. The atomic coordinates of the optimized models can be found in Supplementary Dataset 1.

At high applied overpotentials, the strongly oxidizing reaction conditions lead to carbon atoms being covered by adsorbed oxygen, significantly affecting the catalytic properties. We therefore calculated binding free energies of \*O ( $\Delta G_{*O}$ ) on top and below the graphene sheet at different oxidation states referenced to the free energies of the H<sub>2</sub> and H<sub>2</sub>O gas phase molecules. To investigate the effect of surface adsorbed \*O on catalytic activity, we calculated the \*O coverage-dependent \*OH binding free energies ( $\Delta G_{*OH}$ ), which is a key intermediate in electrochemical H<sub>2</sub>O oxidation to H<sub>2</sub>O<sub>2</sub> (ref. 13).

To convert the calculated electronic energies into free energies, we added free-energy corrections for adsorbates, which include the zero-point energy, enthalpy and entropy at 300 K, using the harmonic oscillator approximation. For gaseous molecules, we used the ideal gas approximation with partial pressures of 101,325 Pa for H<sub>2</sub> and 3,534 Pa for H<sub>2</sub>O, which is the vapour pressure of H<sub>2</sub>O. The effect of potential was included using the computational hydrogen electrode method<sup>55</sup>, where the chemical potential of the proton and electron pair equals half of that of hydrogen gas ( $\mu(\text{H}^+ + e^-) = \frac{1}{2}\mu(\text{H}_2)$ ) at standard conditions. As the potential is applied, the chemical potential of an electron is shifted by  $-eU_{\text{elec}}$ , where  $e$  and  $U_{\text{elec}}$  are elementary charge and electrode potential, respectively.

## Data availability

The data that support the plots within this paper and other findings of this study are available from the corresponding authors on reasonable request.

Received: 15 July 2019; Accepted: 14 November 2019;

Published online: 06 January 2020

## References

- Perry, S. C. et al. Electrochemical synthesis of hydrogen peroxide from water and oxygen. *Nat. Rev. Chem.* **3**, 442–458 (2019).
- Shen, R. et al. High-concentration single atomic Pt sites on hollow CuS<sub>x</sub> for selective O<sub>2</sub> reduction to H<sub>2</sub>O<sub>2</sub> in acid solution. *Chem* **5**, 2009–2110 (2019).
- Campos-Martin, J. M., Blanco-Brieva, G. & Fierro, J. L. Hydrogen peroxide synthesis: an outlook beyond the anthraquinone process. *Angew. Chem. Int. Ed.* **45**, 6962–6984 (2006).
- Kuttassery, F. et al. One electron-initiated two-electron oxidation of water by aluminum porphyrins with earth's most abundant metal. *ChemSusChem* **10**, 1909–1915 (2017).
- Remello, S. N. et al. Two-electron oxidation of water to form hydrogen peroxide catalysed by silicon-porphyrins. *Sustain. Energy Fuels* **2**, 1966–1973 (2018).
- Mathew, S. et al. Two-electron oxidation of water through one-photon excitation of aluminium porphyrins: molecular mechanism and detection of key intermediates. *ChemPhotoChem* **2**, 240–248 (2018).
- Yang, S. et al. Toward the decentralized production of H<sub>2</sub>O<sub>2</sub>: a focus on the catalysis. *ACS Catal.* **8**, 4064–4081 (2018).
- Edwards, J. K. & Hutchings, G. J. Palladium and gold-palladium catalysts for the direct synthesis of hydrogen peroxide. *Angew. Chem. Int. Ed.* **47**, 9192–9198 (2008).
- Kim, H. W. et al. Efficient hydrogen peroxide generation using reduced graphene oxide-based oxygen reduction electrocatalysts. *Nat. Catal.* **1**, 282–290 (2018).
- Lu, Z. et al. High-efficiency oxygen reduction to hydrogen peroxide catalysed by oxidized carbon materials. *Nat. Catal.* **1**, 156–162 (2018).
- Siahrostami, S. et al. Enabling direct H<sub>2</sub>O<sub>2</sub> production through rational electrocatalyst design. *Nat. Mater.* **12**, 1137–1143 (2013).
- Izgorodin, A., Izgorodina, E. & MacFarlane, D. R. Low overpotential water oxidation to hydrogen peroxide on a MnOx catalyst. *Energy Environ. Sci.* **5**, 9496–9501 (2012).
- Shi, X. et al. Understanding activity trends in electrochemical water oxidation to form hydrogen peroxide. *Nat. Commun.* **8**, 701 (2017).
- Kelly, S. et al. ZnO as an active and selective catalyst for electrochemical water oxidation to hydrogen peroxide. *ACS Catal.* **9**, 4593–4599 (2019).
- Han, L. et al. In-plane carbon lattice-defect regulating electrochemical oxygen reduction to hydrogen peroxide production over nitrogen-doped graphene. *ACS Catal.* **9**, 1283–1288 (2019).
- Zhao, K. et al. Enhanced H<sub>2</sub>O<sub>2</sub> production by selective electrochemical reduction of O<sub>2</sub> on fluorine-doped hierarchically porous carbon. *J. Catal.* **357**, 118–126 (2018).
- Jiang, Y. et al. Selective electrochemical H<sub>2</sub>O<sub>2</sub> production through two-electron oxygen electrochemistry. *Adv. Energy Mater.* **8**, 1801909 (2018).
- Fuku, K., Miyase, Y., Miseki, Y., Gunji, T. & Sayama, K. Enhanced oxidative hydrogen peroxide production on conducting glass anodes modified with metal oxides. *ChemistrySelect* **1**, 5721–5726 (2016).
- Kanan, M. W. & Nocera, D. G. In situ formation of an oxygen-evolving catalyst in neutral water containing phosphate and Co<sup>2+</sup>. *Science* **321**, 1072–1075 (2008).
- Finke, C. E. et al. Enhancing the activity of oxygen-evolution and chlorine-evolution electrocatalysts by atomic layer deposition of TiO<sub>2</sub>. *Energy Environ. Sci.* **12**, 358–365 (2019).
- Song, F. & Hu, X. Exfoliation of layered double hydroxides for enhanced oxygen evolution catalysis. *Nat. Commun.* **5**, 4477 (2014).
- Suntivich, J., May, K. J., Gasteiger, H. A., Goodenough, J. B. & Shao-Horn, Y. A perovskite oxide optimized for oxygen evolution catalysis from molecular orbital principles. *Science* **334**, 1383–1385 (2011).
- McCrorry, C. C., Jung, S., Peters, J. C. & Jaramillo, T. F. Benchmarking heterogeneous electrocatalysts for the oxygen evolution reaction. *J. Am. Chem. Soc.* **135**, 16977–16987 (2013).
- Zhang, B. et al. Homogeneously dispersed multimetal oxygen-evolving catalysts. *Science* **352**, 333–337 (2016).
- Zheng, X. et al. Theory-driven design of high-valence metal sites for water oxidation confirmed using in situ soft X-ray absorption. *Nat. Chem.* **10**, 149–154 (2018).
- Viswanathan, V., Hansen, H. A. & Nørskov, J. K. Selective electrochemical generation of hydrogen peroxide from water oxidation. *J. Phys. Chem. Lett.* **6**, 4224–4228 (2015).
- Park, S. Y. et al. CaSnO<sub>3</sub>: an electrocatalyst for two-electron water oxidation reaction to form H<sub>2</sub>O<sub>2</sub>. *ACS Energy Lett.* **4**, 352–357 (2018).
- Xu, W., Lu, Z., Wan, P., Kuang, Y. & Sun, X. High-performance water electrolysis system with double nanostructured superaerophobic electrodes. *Small* **12**, 2492–2498 (2016).
- Lu, Z. et al. Superaerophilic carbon-nanotube-array electrode for high-performance oxygen reduction reaction. *Adv. Mater.* **28**, 7155–7161 (2016).
- Yu, C., Zhang, P., Wang, J. & Jiang, L. Superwettability of gas bubbles and its application: from bioinspiration to advanced materials. *Adv. Mater.* **29**, 1703053 (2017).
- Lv, K. et al. Hydrophobic and electronic properties of the E-MoS<sub>2</sub> nanosheets induced by FAS for the CO<sub>2</sub> electroreduction to syngas with a wide range of CO/H<sub>2</sub> ratios. *Adv. Funct. Mater.* **28**, 1802339 (2018).
- Tang, C., Cheng, N., Pu, Z., Xing, W. & Sun, X. NiSe nanowire film supported on nickel foam: an efficient and stable 3D bifunctional electrode for full water splitting. *Angew. Chem. Int. Ed.* **54**, 9351–9355 (2015).

33. Wang, J., Zhong, Hx, Qin, Yl & Zhang, Xb An efficient three-dimensional oxygen evolution electrode. *Angew. Chem. Int. Ed.* **52**, 5248–5253 (2013).
34. Park, S. Y. et al.  $\text{CaSnO}_3$ : an electrocatalyst for 2-electron water oxidation reaction to form  $\text{H}_2\text{O}_2$ . *ACS Energy Lett.* **4**, 352–357 (2018).
35. Fuku, K. & Sayama, K. Efficient oxidative hydrogen peroxide production and accumulation in photoelectrochemical water splitting using a tungsten trioxide/bismuth vanadate photoanode. *Chem. Commun.* **52**, 5406–5409 (2016).
36. Shi, X., Zhang, Y., Siahrostami, S. & Zheng, X. Light-driven  $\text{BiVO}_4$ -C fuel cell with simultaneous production of  $\text{H}_2\text{O}_2$ . *Adv. Energy Mater.* **8**, 1801158 (2018).
37. Coplen, T. B. Normalization of oxygen and hydrogen isotope data. *Chem. Geol.* **72**, 293–297 (1988).
38. Harris, P. Fullerene-related structure of commercial glassy carbons. *Philos. Mag.* **84**, 3159–3167 (2004).
39. Chen, S. et al. Defective carbon-based materials for the electrochemical synthesis of hydrogen peroxide. *ACS Sust. Chem. Eng.* **6**, 311–317 (2017).
40. Siahrostami, S. & Vojvodic, A. Influence of adsorbed water on the oxygen evolution reaction on oxides. *J. Phys. Chem. C* **119**, 1032–1037 (2014).
41. Casalogue, H. S. et al. Direct observation of the oxygenated species during oxygen reduction on a platinum fuel cell cathode. *Nat. Commun.* **4**, 2817 (2013).
42. Karlberg, G. & Wahnström, G. Density-functional based modeling of the intermediate in the water production reaction on Pt (111). *Phys. Rev. Lett.* **92**, 136103 (2004).
43. Patel, A. M. et al. Theoretical approaches to describing the oxygen reduction reaction activity of single atom catalysts. *J. Phys. Chem. C* **122**, 29307–29318 (2018).
44. Mathew, K., Sundararaman, R., Letchworth-Weaver, K., Arias, T. & Hennig, R. G. Implicit solvation model for density-functional study of nanocrystal surfaces and reaction pathways. *J. Chem. Phys.* **140**, 084106 (2014).
45. Yan, H., Xu, B., Shi, S. & Ouyang, C. First-principles study of the oxygen adsorption and dissociation on graphene and nitrogen doped graphene for Li-air batteries. *J. Appl. Phys.* **112**, 104316 (2012).
46. Ni, S., Li, Z. & Yang, J. Oxygen molecule dissociation on carbon nanostructures with different types of nitrogen doping. *Nanoscale* **4**, 1184–1189 (2012).
47. He, G., Liang, T., Wang, Q., Xu, M. & Liu, Y. Increased permeability of oxygen atoms through graphene with ripples. *Soft Matter* **13**, 3994–4000 (2017).
48. McKillop, A. & Sanderson, W. R. Sodium perborate and sodium percarbonate: further applications in organic synthesis. *J. Chem. Soc. Perkin Trans. I* **1**, 471–476 (2000).
49. Jiang, K. et al. Transition-metal single atoms in a graphene shell as active centers for highly efficient artificial photosynthesis. *Chem* **3**, 950–960 (2017).
50. Han, N. et al. Nitrogen-doped tungsten carbide nanoarray as an efficient bifunctional electrocatalyst for water splitting in acid. *Nat. Commun.* **9**, 924 (2018).
51. Kresse, G. & Joubert, D. From ultrasoft pseudopotentials to the projector augmented-wave method. *Phys. Rev. B* **59**, 1758 (1999).
52. Kresse, G. & Furthmüller, J. Efficiency of ab-initio total energy calculations for metals and semiconductors using a plane-wave basis set. *Comput. Mater. Sci.* **6**, 15–50 (1996).
53. Wellendorff, J. et al. Density functionals for surface science: exchange-correlation model development with Bayesian error estimation. *Phys. Rev. B* **85**, 235149 (2012).
54. Blöchl, P. E. Projector augmented-wave method. *Phys. Rev. B* **50**, 17953 (1994).
55. Nørskov, J. K. et al. Origin of the overpotential for oxygen reduction at a fuel-cell cathode. *J. Phys. Chem. B* **108**, 17886–17892 (2004).
56. Kim, K.-W., Kuppuswamy, M. & Savinell, R. Electrochemical oxidation of benzene at a glassy carbon electrode. *J. Appl. Electrochem.* **30**, 543–549 (2000).

## Acknowledgements

This work was supported by Rice University. H.W. is a CIFAR Azrieli Global Scholar in the Bio-inspired Solar Energy Programme. C.X. acknowledges support from a J. Evans Attwell-Welch Postdoctoral Fellowship provided by the Smalley-Curl Institute. K.C. acknowledges a grant (9455) from VILLUM FONDEN. S.S. acknowledges the support from the University of Calgary's Canada First Research Excellence Fund Program, the Global Research Initiative in Sustainable Low Carbon Unconventional Resources. S.R. and S.B. acknowledge funding from US Department of Energy, Office of Science, Office of Basic Energy Sciences, Chemical Sciences, Geosciences, and Biosciences Division, Catalysis Science Program to the SUNCAT Center for Interface Science and Catalysis. This work was performed in part at the Shared Equipment Authority (SEA) at Rice University. The authors acknowledge L. Fan for the design of the scheme in Fig. 3. The authors also acknowledge Q. Jiang, T. Sun and Z. Lu for their support to the experiment and useful discussions.

## Author contributions

C.X. and H.W. conceptualized the project. H.W., K.C. and S.S. supervised the project. C.X. synthesized the catalysts, conducted the catalytic tests and the related data processing, and performed materials characterization and analysis with the help of K.J., F.C. and X.S. S.B. and S.R. performed the theoretical study. C.X. and H.W. wrote the manuscript with support from all authors.

## Competing interests

The authors declare no competing interests.

## Additional information

**Supplementary information** is available for this paper at <https://doi.org/10.1038/s41929-019-0402-8>.

**Correspondence and requests for materials** should be addressed to S.S., K.C. or H.W.

**Reprints and permissions information** is available at [www.nature.com/reprints](http://www.nature.com/reprints).

**Publisher's note** Springer Nature remains neutral with regard to jurisdictional claims in published maps and institutional affiliations.

© The Author(s), under exclusive licence to Springer Nature Limited 2020